Supplementary Material

Multimodal Longitudinal Optical Imaging Reveals Optic Neuritis Preceding Retinal Pathology in Experimental Autoimmune Encephalomyelitis

Raphael Raspe[1,2,3], Robert Günther[3], Ralf Uecker[3], Asylkhan Rakhymzhan[3], Friedemann Paul[4,5], Helena Radbruch[1], Raluca Niesner[3], Anja E. Hauser[2,3]

[1]Department of Neuropathology, Charité – Universitätsmedizin Berlin, Berlin, Germany

[2]Charité – Universitätsmedizin Berlin, Department of Rheumatology and Clinical Immunology, , corporate member of Freie Universität Berlin and Humboldt-Universität zu Berlin, 10117 Berlin, Germany

[3]Immune Dynamics, Deutsches Rheuma-Forschungszentrum (DRFZ), a Leibniz Institute, Charitéplatz 1, 10117 Berlin, Germany

[4]NeuroCure Clinical Research Center, Charité – Universitätsmedizin Berlin, Berlin, Germany

[5]Experimental and Clinical Research Center, Charité – Universitätsmedizin Berlin and Max Delbrueck Center for Molecular Medicine, Berlin, Germany

Address correspondence to: Anja E. Hauser, anja.hauser-hankeln@charite.de

Supplementary Material

1. eMethods

1.1 Mice and Experimental Autoimmune Encephalomyelitis (EAE)

One week before the start of experiments, mice were transferred to an animal care facility adjacent to the experimental facilities, where they were held in cages of 2-6 littermates. Male and female mice were immunized by subcutaneous injection of 250 µg of myelin oligodendrocyte glycoprotein peptide MOG_{35-55} (Pepceuticals, UK) emulsified with 850 µg of killed M. tuberculosis H37 Ra (BD Difco, Germany) in 100 µL Complete Freund's Adjuvant (CFA, BD Difco, Germany) and 100 µL phosphate buffered saline solution (PBS) into the tail base and received 200 ng pertussis toxin in 200 µL PBS (PTX, List Biological Laboratories, Inc.) intraperitoneally both at the time of immunization, as well as 48 h later. Control animals received an equal volume of PBS emulsified in CFA, with an identical PTX regime. Mice were weighed and scored daily using a standardized clinical score for motor symptoms (0.0 – no signs, 1.0 – hind limb paresis, 2.0 – hind limb paralysis, 3.0 – hind limb paralysis and additional fore limb paresis, 4.0 – moribund, 5.0 - death).

1.2 Co-registered Two-Photon Laser-Scanning Microscopy and Optical Coherence Tomography (2PM-OCT)

We used a customized laser-scanning microscope based on a commercial scan head (TriMScope II, LaVision BioTec – a Miltenyi company, Bielefeld, Germany). Fluorophores were excited using a near-infrared Titanium:Sapphire laser (Ti:Sa, Chameleon Ultra II, Coherent, Glasgow, UK; emission range 690 nm – 1080 nm) and an optical parametric oscillator (OPO, APE, Berlin, Germany; emission range 1050 nm – 1300 nm). A multi-immersion 10x objective lens with 8 mm working distance (XLPLN10XSVMP, NA = 0.6, Olympus, Hamburg, Germany) was used to focus the excitation beam through the eye lens into the retina. Fluorescence signal detection was accomplished using photomultiplier tubes (PMTs) in the spectral ranges of 466 ± 20 nm, 525 ± 25 nm, and 593 ± 20 nm. Cerulean was excited using the Ti:Sa laser at 850 nm and its fluorescence was detected at 466 ± 20 nm, simultaneously with Citrine fluorescence detected at both 525 ± 25 nm and 593 ± 20 nm. EGFP and Sulforhodamine 101 were simultaneously excited using the Ti:Sa laser at 940 nm and their fluorescence detected at 525 ± 25 nm and 593 ± 20 nm, respectively. tdRFP was excited using the OPO laser at 1100 nm and detected at 593 ± 20 nm. Images were acquired using 4-fold averaging.

The 2PM setup was extended with a spectral domain OCT module based on a system (Ganymede II, Thorlabs, Dachau, Germany) using a super-luminescence light source (SLD, continuous wave laser diode, central wavelength 930 nm). The OCT beam was scanned over the sample using the integrated galvanometric scanner of the two-photon microscope at 50 Hz line rate with 8-fold averaging. The beam was focused into the retina by the same objective lens used for 2PM. The axial resolution of the OCT module amounts to 2 µm.

1.3 Tissue Collection, Immunofluorescent Stainings and Optical Clearing

Immediately after the last imaging session, mice were sacrificed by isoflurane overdose and transcardially perfused using sequentially PBS and 4% paraformaldehyde (PFA). Eyes and optic nerves were removed, incubated in 4% PFA for

1 hr, and shortly stored in PBS. Retinae were separated from other tissues, dissected into clover-shaped flatmounts[1], and stored for up to 1 month in 99% methanol.

For immunofluorescent staining, flatmounts were rehydrated in PBS for 30 min before blocking for 1 hr in 200 μL working solution (0.2% BSA, 5% FCS and 0.03% Triton X-100 in PBS) and subsequently adding 200 μL of the primary antibody mix, consisting of rat anti-GFP-Alexa®488 (BioLegend, San Diego, CA, USA, 1:200), mouse anti-phosphorylated-Neurofilament-H-Biotin (pNF-H, NovusBiologicals, Centennial, CO, USA 1:200), mouse anti-Brn3a-Alexa®594 (SantaCruz, Dallas, TX, USA, 1:50) and rat anti-CD45-Alexa®647 (BioLegend, 1:50) in working solution, for overnight incubation at 4°C. Samples were washed four times for 15 min in working solution, after which 200 μL of the secondary antibody solution, consisting of DAPI (Sigma, 1:1000) and Streptavidin-Alexa®546 (BioLegend, 1:200) in working solution, were added for overnight incubation at 4°C. After four additional rounds of washing, flatmounts were ready for imaging.

Optic nerves were blocked for 1 hr in 200 μL working solution (0.2% BSA, 5% FCS and 0.03% Triton X-100 in PBS) and subsequently stained with 200 μL of rat anti-CD45-Alexa®647 (BioLegend, 1:50) in working solution. For dehydration, optic nerves were then incubated in increasing concentrations of ethanol (50%, 70%, 99%, 99%) at pH = 9 for 30 min each, after which they were transferred into ethyl cinnamate (ECi, Sigma-Aldrich, an affiliate of Merck KGaA, Darmstadt, Germany) for optical clearing. Immediately before imaging, optic nerves were slightly glued onto a plastic surface and placed in a cuvette (LaVision BioTec – a Miltenyi company, Bielefeld, Germany) containing ECi.

1.4 Image Analysis

When necessary for downstream analyses, the exact position of the ONH was manually annotated in images. Whenever user input was required during image analysis, users were blinded by pseudonymization of raw data.

Stitching of LSFM images acquired in multi-position scans of optic nerves, segmentation and counting of CD45+ cells, as well as extraction of raw data for analyzing the spatial distribution thereof, was performed using Imaris 9.9.1 software (Bitplane, Belfast, UK). For identification of CD45+ cells we used the built-in spot detection function in Imaris (spot diameter = 7 μm) after smoothing with a Gaussian filter (radius = 0.271 μm) and background subtraction. For analysis of spatial homogeneity, the value of Ripley's K-function[2] was calculated for a radius of 50 μm, i.e. the mean number of CD45+ cells within a 50 μm radius of a given cell was divided by the overall density of cells per μm³ of optic nerve, with lower K values indicating a more homogenous distribution. For clustering, conglomerates of five or more cells were considered clusters if for each cell within the conglomerate the distance to the nearest neighbour within the conglomerate was no larger 14 μm (i.e., twice the input diameter used for CD45+ cell segmentation). Calculation of Ripley's K and clustering of CD45+ cells were performed using custom-written algorithms in Jupyter Lab[3].

To account for the worse axial compared to lateral resolution in 2PM, the 3D volumes acquired by co-registered 2PM-OCT were re-scaled assuming vessel cross-sections to be circular in the retina. Within this field of view acquired by 2PM-OCT, all analyses were limited to the areas or volumes sufficiently well illuminated, with subsequent quantitative results being accordingly normalized to the area or volume considered for analysis.

A graphical depiction of the workflow used for OCT data analysis is shown in eFigure 3A. Raw OCT data were denoised using the machine-learning N2V algorithm[4] (N2V plugin for ImageJ, v0.8.6) with a model previously trained on a randomly selected subset of the data (34 volumes, 504 × 505 × 512 pixels, 300 epochs). For each acquired volume, a sufficiently well illuminated rectangular region of interest in xy was chosen for further analysis. A minimum of 3000 A-scans continuously covering the whole region of interest in serpentines was then projected as a 2D image for semi-automated segmentation and quantification of IRL thickness, using existing plugins in FIJI. IRL thickness physiologically decreases with distance from ONH and was subject to considerable interindividual variation. For data standardization, the IRL thickness for each volume at any given distance from ONH was expressed as the difference from mean IRL thickness at the respective distance from ONH, with all measurements in one mouse considered for calculation of the mean.

FRET efficiency of the TN-L15 construct in neurons was calculated in data acquired in the retinae of *CerTNL-15* mice as previously described[5]. Briefly, intensity (I) values of the three acquisition channels (466 ± 20, 525 ± 25, and 593 ± 20 nm) were smoothed with a Gaussian filter and corrected for background (B), spectral sensitivity (η) of the PMTs and spectral overlap (α) of Cerulean and Citrine fluorescence in the 525 ± 25 nm, and 593 ± 20 nm detection channels. Thus, relative acceptor FRET signal was calculated as follows:

$$FRET_{acceptor} = \frac{I_{Citrine}}{I_{Citrine} + I_{Cerulean}} = \frac{\frac{\alpha_{525}}{\eta_{525}} \cdot (I_{525} - B_{525}) + \frac{\alpha_{593}}{\eta_{593}} \cdot (I_{593} - B_{593})}{\frac{\alpha_{466}}{\eta_{466}} \cdot (I_{466} - B_{466}) + \frac{\alpha_{525}}{\eta_{525}} \cdot (I_{525} - B_{525}) + \frac{\alpha_{593}}{\eta_{593}} \cdot (I_{593} - B_{593})}$$

Mean FRET efficiency was calculated for all pixels belonging to Thy1$^+$ cells (thresholded using signal intensity in the 525 ± 25 channel). To account for interindividual differences in baseline FRET efficiency, results were expressed in relation to the baseline FRET ratio measured on day -3 prior to immunization.

Brn3a$^+$ somata of retinal ganglion cells were segmented and counted in retinal flatmounts using the existing pre-trained machine-learning cell segmentation algorithm StarDist[6] (StarDist 2D plugin, v0.3.0, in FIJI). pNF-H$^+$ somata of retinal ganglion cells were manually counted in retinal flatmounts by a blinded observer. Using the same pNF-H stain, axonal damage in individual images was scored by a blinded observer using the following score: 0 – no axonal stain, or only evenly stained axons without signs of axonal beading; 1 – Occasional axonal beads, and/or occasional jumps in axonal calibre, and/or occasional open-ended axons; 2 – axonal beading in a majority of stained axons, or multiple severely affected axons; 3 – axonal beading in virtually all axons, and majority of axons severely affected. Individual scores of four images from central or peripheral retinal areas, respectively, were added for a final score reaching from 0 to 12.

Raw 2PM data acquired *in vivo* in *CX3CR1.EGFP$^{+/-}$* mice were denoised using the N2V[4] plugin for FIJI with a model previously trained for 300 epochs on 76 independently acquired z-stacks (505 × 505 × 25 pixels). Due to high ramification of EGFP$^+$ surfaces, we chose not to perform single cell segmentation, but rather limited our analysis to the segmentation of EGFP$^+$ voxels, making use of the Phansalkar[7] local thresholding algorithm, as well as of the ImageJ 3D Suite[8]. Perivascular cell surfaces were defined by a distance of ≤ 10 μm from Srh101-stained blood vessels.

To determine the spatial orientation of EGFP$^+$ surfaces, we used the Edge Detection plugin in ImageJ[9]. Edge voxels were considered aligned if the spatial orientation of the respective edge differed less than ±20° from the polar angle of the

edge, using a polar coordinate system with the ONH as pole for reference (as illustrated in Fig. 5C). Thus, within a population of randomly oriented cells, stochastically, a fraction of $\frac{40}{180} = 0.22$ would be expected to be aligned. Conversely, a population of more radially aligned cells would be expected to yield a substantially higher aligned fraction.

TrackMate[10] (Trackmate plugin for FIJI, v7.10.2) was used to track EGFP$^+$ surfaces. To facilitate tracking of EGFP$^+$ cell motility, we subtracted the intensity values of each frame t_n from the following frame t_{n+1}, thus eliminating all stationary cells (which would have otherwise impeded robust analysis) from further consideration and tracking only the remaining cells that had moved during the acquisition of each two consecutive frames (eFigure 8C). Thus, track statistics calculated and displayed herein only include motile EGFP$^+$ cells, not non-migratory ones. To avoid tracking errors due to breathing-caused motion artifacts, we limited the algorithmic gap-closing to 45 μm per frame, which in turn resulted in a maximum trackable velocity of 30 μm/min. For each cell trajectory, we additionaly calculated the radial displacement by subtracting the distance to the ONH of its starting point from that of its end point, with positive values indicating movement from and negative values indicating movement towards the ONH (see eFigure 5C). Unless otherwise stated, displacement data presented herein represent aggregate displacement (i.e., the overall movement of all cells registered per minute of acquisition in one volume).

TrackMate was also used to identify and track tdRFP$^+$ cells in *LysM.tdRFP* mice. Because tdRFP$^+$ cells were less ramified, we were able to track the motility of all cells, also including the non-migratory ones. Other than that, parameters used for tracking remained the same as for EGFP$^+$ cells.

1.5 Statistical Analysis

Because this study was explorative, no *a priori* calculation of sample sizes was performed. No randomization took place to assign experimental groups. We did not control for potential confounders such as treatment/measurement order, cage location or daytime of measurements. Experimentators were not blinded while performing in-vivo imaging but were blinded in data analysis whenever it was not automated. Mice or single eyes were excluded from analysis if routine clinical assessment or post-mortem dissection revealed ocular malformations or signs of anterior uveitis. Specifically, one mouse from the EAE group was excluded due ectopic growth of retinal epithelium into the vitreous body of both eyes; the non-imaged eye of one control animal was excluded due to the same reason. Individual measurement timepoints had to be excluded from analysis in case of technical malfunction of parts of the imaging setup. Our standardized measurement locations in flatmount histology were sometimes missing due to tears during tissue preparation.

1.6 Supplementary References

1. Tual-Chalot S, Allinson KR, Fruttiger M, Arthur HM. Whole mount immunofluorescent staining of the neonatal mouse retina to investigate angiogenesis in vivo. Journal of visualized experiments : JoVE. 2013:e50546.
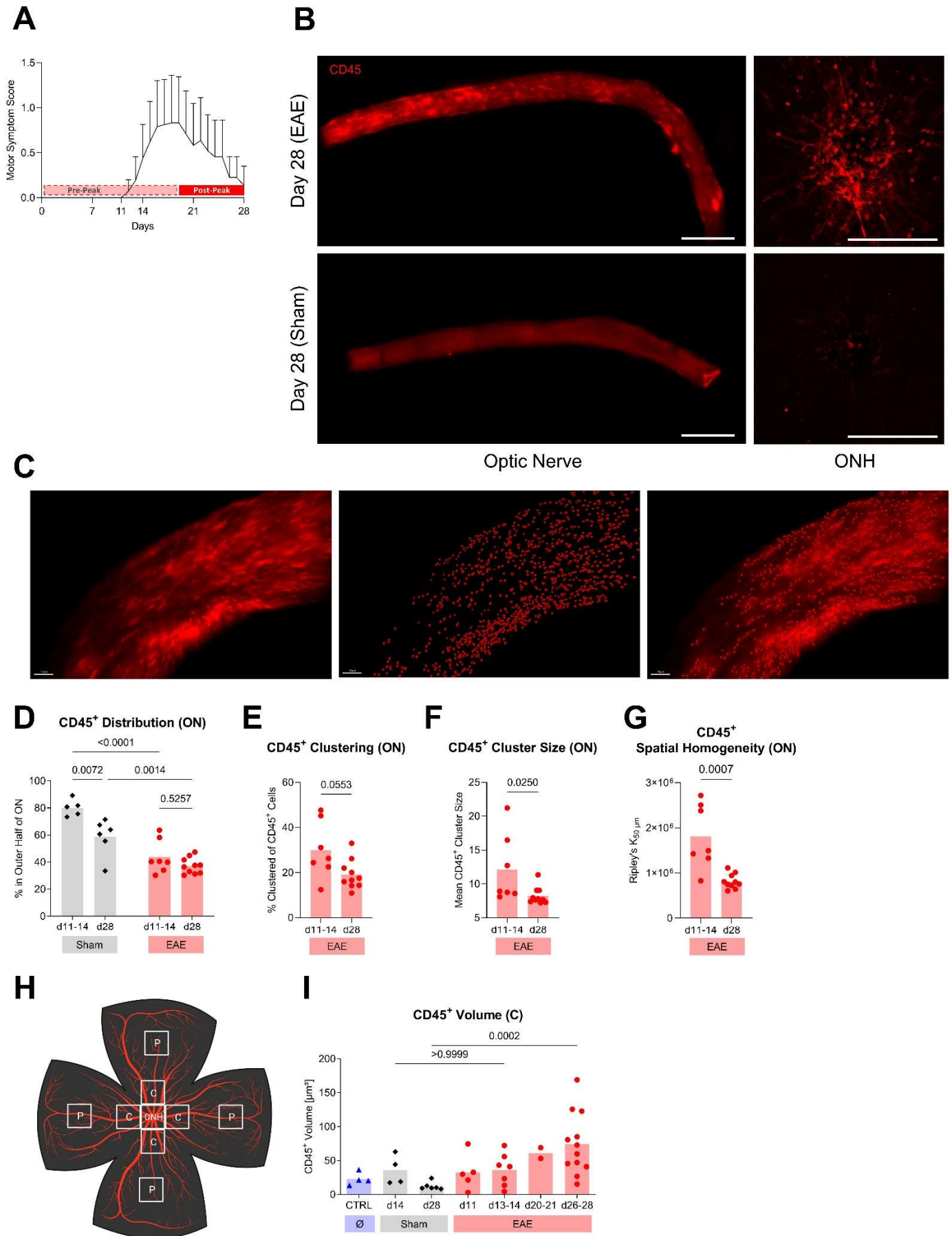
2. Ripley BD. The second-order analysis of stationary point processes. Journal of Applied Probability. 1976;13:255–266.

3. Darian A, Granger B, Grout J, Pérez F, Ruvalcaba A, Silvester S. Project Jupyter [online]. Available at: github.com/jupyter. Accessed April 14, 2024, 15:08.

4. Krull A, Buchholz T-O, Jug F. Noise2Void - Learning Denoising from Single Noisy Images; 2018. Available at: arxiv.org/pdf/1811.10980v2.

5. Bremer D, Pache F, Gunther R, et al. Longitudinal Intravital Imaging of the Retina Reveals Long-term Dynamics of Immune Infiltration and Its Effects on the Glial Network in Experimental Autoimmune Uveoretinitis, without Evident Signs of Neuronal Dysfunction in the Ganglion Cell Layer. Front Immunol. 2016;7:642.

6. Schmidt U, Weigert M, Broaddus C, Myers G. Cell Detection with Star-Convex Polygons. In: Frangi AF, Schnabel JA, Davatzikos C, Alberola-López C, Fichtinger G, editors. Medical Image Computing and Computer Assisted Intervention – MICCAI 2018. Lecture Notes in Computer Science. Cham: Springer International Publishing; 2018. p. 265–73.

7. Phansalkar N, More S, Sabale A, Joshi M. Adaptive local thresholding for detection of nuclei in diversity stained cytology images. In: 2011 International Conference on Communications and Signal Processing. 2011 International Conference on Communications and Signal Processing (ICCSP); Feb. 10-12, 2011; Kerala, India: IEEE; 022011. p. 218–20.

8. Ollion J, Cochennec J, Loll F, Escudé C, Boudier T. TANGO: a generic tool for high-throughput 3D image analysis for studying nuclear organization. Bioinformatics. 2013;29:1840–1841.

9. Boudier T. Edge Detection: Edge Detection by Canny-Deriche filtering [online]. Available at: imagejdocu.list.lu/plugin/filter/edge_detection/start. Accessed January 31, 2024, 13:41.

10. Tinevez J-Y, Perry N, Schindelin J, et al. TrackMate: An open and extensible platform for single-particle tracking. Methods. 2017;115:80–90.

2. eTables

eTable 1: Clinical Scores and Optic Nerve Infiltration at Day 28

ID	Cumulative Clinical Score (Area Under the Curve)	CD45$^+$ Optic Nerve Infiltration (M Cells per mm³)
EAE-28-1	15.5	32.3
EAE-28-2	2.25	42.9
EAE-28-3	0.75	45.4
EAE-28-4	11.75	17.5
EAE-28-5	13.25	35.2
EAE-28-6	0	49.8
EAE-28-7	0	38.8
EAE-28-8	13	30.8
EAE-28-9	9.25	41.7
EAE-28-10	27.75	40.0

3. eFigures

eFigure 1: Clinical Scores, Optic Nerve and Retinal Leukocyte Infiltration (Legend on the following page)

eFigure 1: Clinical Scores, Optic Nerve and Retinal Leukocyte Infiltration

A, Graph shows mean clinical motor symptom scores for experimental autoimmune encephalomyelitis (EAE) mice. Based on these clinical data, in vivo measurements at days 7-14 were considered pre-peak and days 21-28 were considered post-peak for EAE mice. Bars represent upper 95%-confidence intervals. n = 19 mice overall, n = 11 remaining at day 28. **B,** Maximum projections of representative light sheet fluorescence microscopy images of optic nerves (left panels) and confocal microscopy images in the optic nerve head (ONH) region of retinal flatmounts (right panels) from an EAE (upper panels) and sham injected (lower panels) mouse at 28 days post induction. $CD45^{+}$ leukocytes are shown in red. Scale bar represents 500 μm in optic nerve images and 200 μm in retinal flatmount images. **C,** Representative light sheet fluorescence microscopy image of the optic nerve of an experimental autoimmune encephalomyelitis (EAE) mouse at day 28 post induction stained for $CD45^{+}$ surfaces (red). Left panel shows volume with original stain, middle panel shows result of spot segmentation (diameter = 7μm) to identify cells, right panel shows superimposition. Scale bars represent 50 μm. **D,** Graph shows percentage of $CD45^{+}$ cells located in the outer half (volume-based) of optic nerves of sham injected and EAE mice sacrificed at the indicated days post induction. **E,** Graph shows percentage clustered of CD45+ cells in optic nerves of EAE mice sacrificed at the indicated days post induction (see Supplementary Methods for definition of a cluster). **F,** Graph shows mean cluster size for clustered CD45+ cells in optic nerves of EAE mice sacrificed at the indicated days post induction. **G,** Graph shows spatial homogeneity of CD45+ cell distribution in optic nerves of EAE mice sacrificed at the indicated days post induction. Spatial homogeneity is expressed as Ripley's $K_{50\ \mu m}$, with lower K values indicating a more homogenous distribution (see Supplementary Methods). **H,** Sketch shows design of retinal flatmount immunofluorescent confocal microscopy imaging. Z-stacks with a z-step of 1 μm were acquired at the optic nerve head region (ONH), the immediately adjacent central retina (C), as well as one stack per flap of peripheral retina (P). Sketch created with Biorender.com. **I,** Graph shows measurements of $CD45^{+}$ volume in central retinal flatmount areas of untreated control, sham injected and EAE mice, the latter two having been sacrificed at the indicated days post injection. Datapoints in **D-G** and **I** represent means of measurements in left and right optic nerve/retina. Bars represent means. Statistical significance was determined by repeated measures two-way ANOVA with subsequent Šídák's multiple comparisons test in **D,** two-tailed Mann-Whitney test in **E-G**, and Kruskal-Wallis test with subsequent Dunn's multiple comparisons test in **I**.
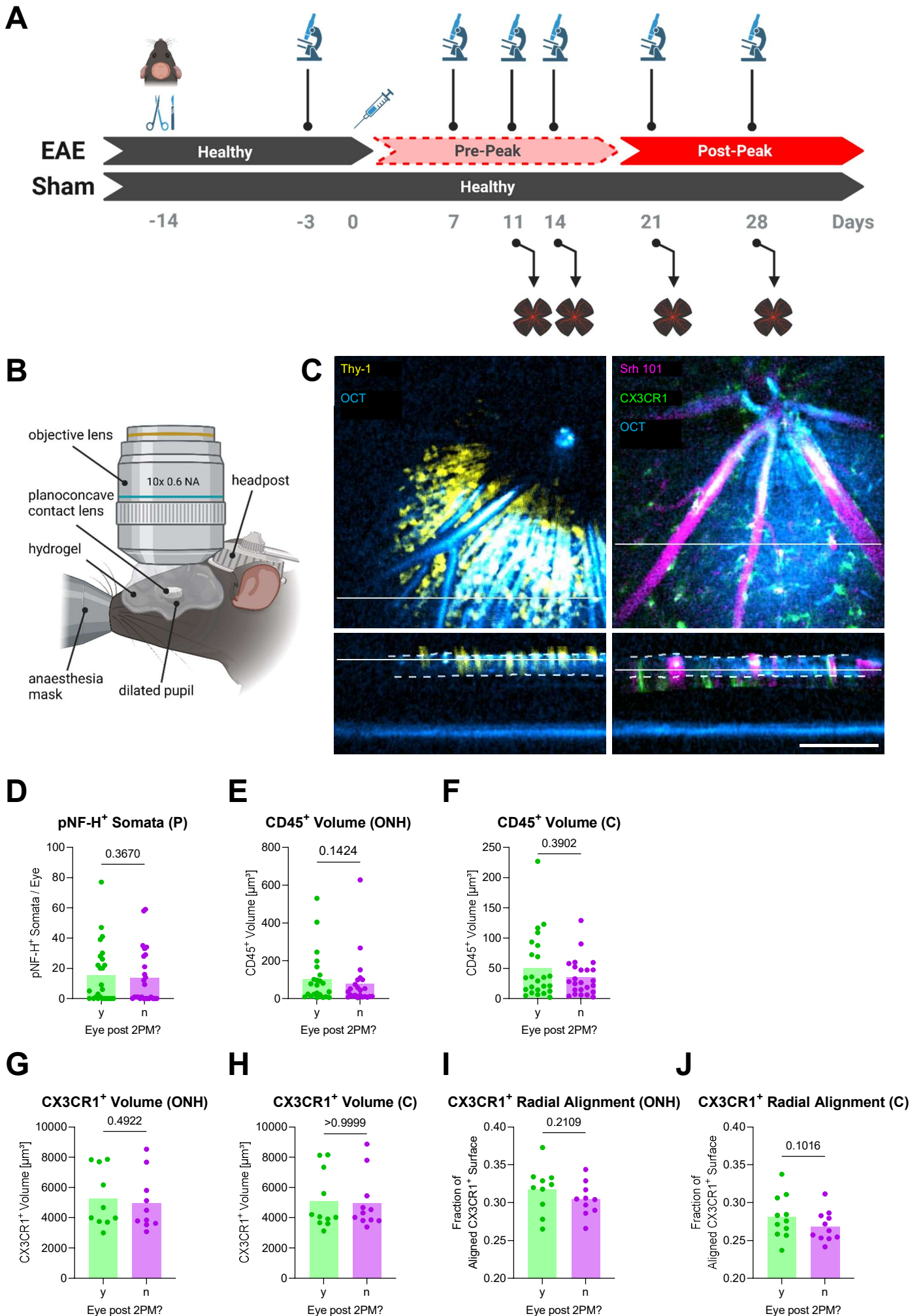
eFigure 2: Experimental Design and Safety of Retinal In Vivo Imaging (Legend on the following page)

eFigure 2: Experimental Design and Safety of Retinal In Vivo Imaging

A, Diagram shows experimental design of longitudinal in vivo imaging. 14 days before induction of experimental autoimmune encephalomyelitis (EAE), or sham injection, respectively, mice underwent headpost surgery. Combined intravital two-photon microscopy and optical coherence tomography (2PM-OCT) was performed on days -3, 7, 11, 14, 21 and 28. Mice were sacrificed and retinal flatmounts were prepared on days 11, 14, 21 and 28. Color-coded arrows indicate how mice were grouped for further analysis of in vivo data. Sketch created with Biorender.com. **B,** Sketch shows the imaging setup. All imaging experiments were performed in inhalation anaesthesia. Using a screw, mice were attached via their headpost to a stage allowing for movement along three translational and two rotational axes. A hydrogel column was applied on top of a planoconcave contact lens placed on the mouse pupil. A water immersion objective was used for imaging. Sketch created with Biorender.com. **C,** Superimposition of representative 2PM-OCT images taken in a healthy *CerTN-L15* mouse (left panel) and a healthy *CX3CR1.EGFP* mouse (right panel), shown in xy (upper panel) and xz (lower panel) planes. White horizontal lines show the position of the respective other plane in each volume. Dashed white lines represent semiautomated IRL segmentation results. Upper OCT images are en face, lower images are cross-sectional. Thy-1$^+$ retinal ganglion cell somata and axons are shown in yellow. OCT intensity values are displayed in shades of cyan. Blood vessels, shown in magenta, were stained by intravenous injection of sulforhodamine 101 (Srh 101). CX3CR1$^+$ microglia, monocytes and macrophages are shown in green. Scale bar represents 200 μm. **D,** Graph compares pNF-H$^+$ retinal ganglion cell (RGC) somata counts in peripheral retinal flatmount areas for pairs of eyes with or without exposition to two-photon imaging (2PM). **E,** Graph compares measurements of CD45$^+$ volume in the optic nerve head (ONH) region of retinal flatmounts for pairs of eyes with or without exposition to 2PM. **F,** Graph compares measurements of CD45$^+$ volume in central retinal flatmount areas for pairs of eyes with or without exposition to 2PM. **G,** Graph compares measurements of CX3CR1$^+$ volume in the ONH region of retinal flatmounts for pairs of eyes with or without exposition to 2PM. **H,** Graph compares measurements of CX3CR1$^+$ volume in central retinal flatmount areas for pairs of eyes with or without exposition to 2PM. **I,** Graph compares measurements of CX3CR1$^+$ surface radial alignment (see "Methods") in the ONH region of retinal flatmounts for pairs of eyes with or without exposition to 2PM. **J,** Graph compares measurements of CX3CR1$^+$ surface alignment in central retinal flatmount areas for pairs of eyes with or without exposition to 2PM. Bars in represent means. Statistical significance was determined by two-tailed Wilcoxon matched-pairs signed rank test.
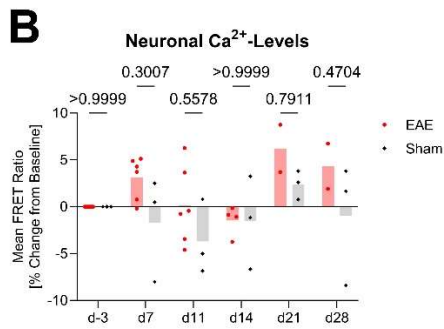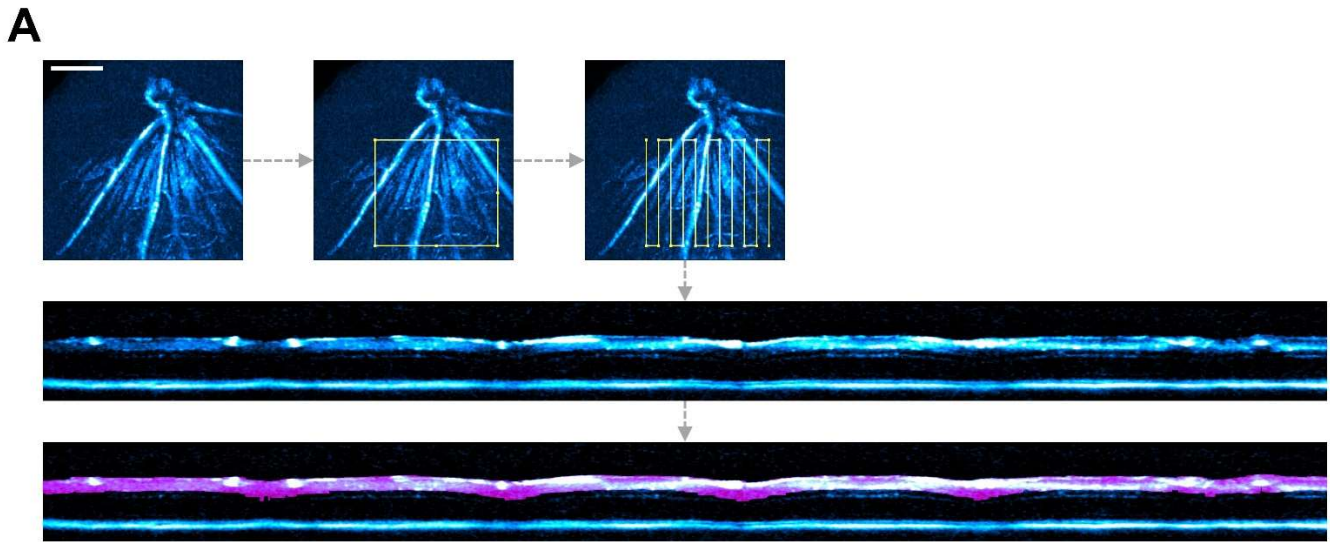
eFigure 3: OCT Image Analysis and Neuronal Calcium Imaging

A, Flowchart exemplifies the process used for analysis of OCT images. After acquisition of three-dimensional volumes (upper left panel, en face projection of the RNFL), a region of interest (ROI) with sufficient image quality was chosen on an en face projection of the RNFL for further analysis by a blinded observer (upper middle panel). A continuous line selection covering the whole ROI in serpentines (upper right panel) was automatically set to reslice the volume into a two-dimensional cross-sectional image consisting of at least 3000 individual A-scans (middle panel), which was used for semi-automated segmentation of the upper retinal layers (lower panel). Scale bar indicates 200 µm. **B,** Graph shows change of mean ratiometric FRET efficiency compared to baseline measurements. Data from Fig. 2C is broken down to single days post EAE induction. Statistical significance was determined by ordinary two-way ANOVA with subsequent Šídák's multiple comparisons test.
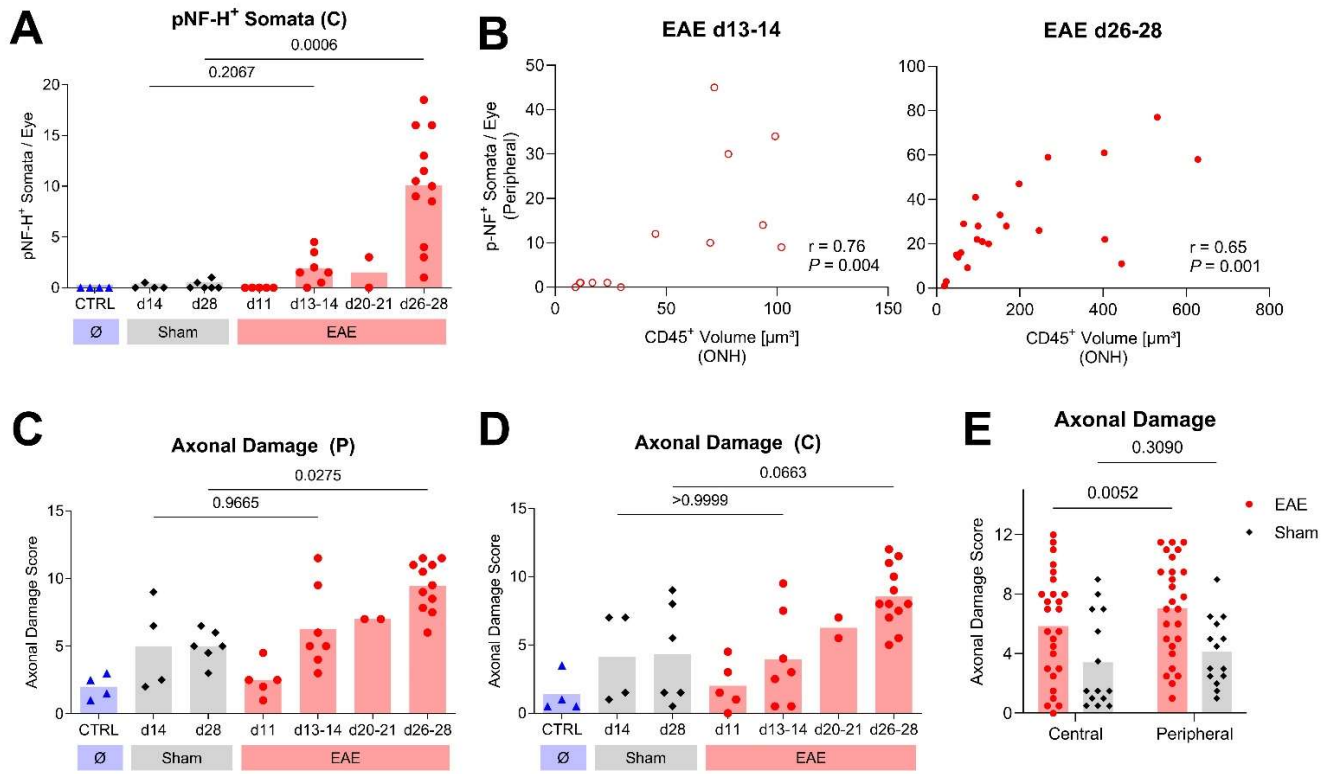
eFigure 4: Histological Evidence of Retinal Ganglion Cell Damage

A, Graph shows pNF-H+ retinal ganglion cell (RGC) somata counted per eye in central retinal areas of untreated control, sham injected and EAE mice, the latter two having been sacrificed at the indicated days post EAE induction. **B,** Graphs show correlation of CD45+ volume in the ONH region and pNF-H+ RGC somata counted per eye in peripheral retinal areas of EAE mice at 13-14 days (left panel) and 26-28 days (right panel) post induction. **C,** Graph shows axonal damage in peripheral retinal areas of untreated control, sham injected and EAE mice, as scored according to the pattern of axonal pNF-H+ accumulation (see Supplementary Methods for details). **D,** Graph shows axonal damage in central retinal areas of untreated control, sham injected and EAE mice, as scored according to the pattern of axonal pNF-H+ accumulation (see Supplementary Methods for details). **E,** Graph shows axonal damage in central and peripheral retinal areas of the same mouse, as scored according to the pattern of axonal pNF-H+ accumulation. Datapoints represent means of measurements in left and right retina. Bars in **A** and **C-E** represent means. Statistical significance was determined by Kruskal-Wallis test with subsequent Dunn's multiple comparisons test in **A** and **C-D,** two-tailed Spearman's correlation in **B**, and ordinary two-way ANOVA with subsequent Šídák's multiple comparisons test in **E**.
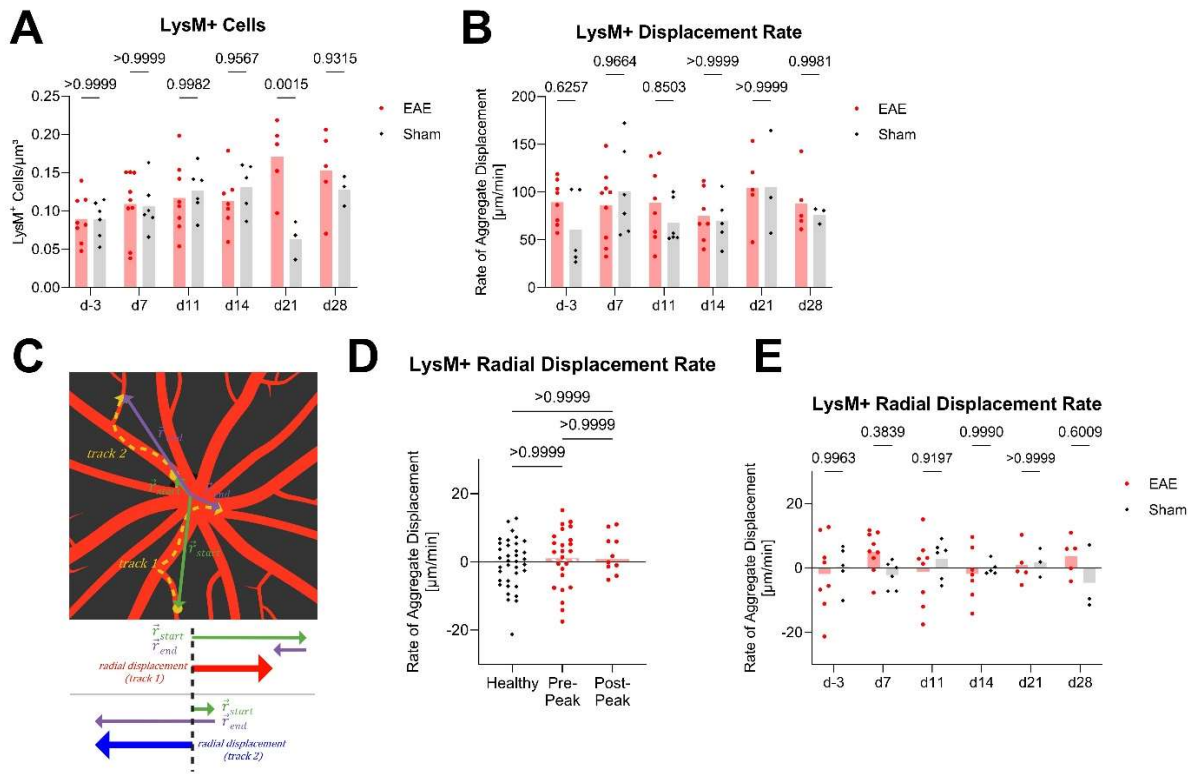
eFigure 5: In Vivo Retinal Phagocyte Quantification and Tracking

A, Graph shows number of LysM+ phagocytes per µm³. Data from Fig. 4B is broken down to single days post induction. **B,** Graph shows displacement rate of LysM⁺ cells. Individual datapoints represent aggregate displacement rate of all LysM⁺ cells registered over the course of one imaging session. Data from Fig. 4D is broken down to single days post injection. **C,** Sketch illustrates calculation of radial displacement for LysM⁺ single cell trajectories. Using a polar coordinate system with the optic nerve head (ONH) as pole, the radial displacement of a track was calculated by subtracting the radial distance of the track's start from the radial distance of its end point (ignoring their respective azimuth). Thus, positive values represent overall displacement towards the retinal periphery, while negative values represent ONH-directed displacement. Sketch created with Biorender.com. **D,** Graph shows radial displacement rate of LysM⁺ cells. Individual datapoints represent aggregate radial displacement rate of all LysM⁺ cells registered over the course of one imaging session. Individual measurements are grouped as indicated in eFigure 2A. **E,** Data from **D** is broken down to single days post induction. Bars represent means. Statistical significance was determined by ordinary two-way ANOVA with subsequent Šídák's multiple comparisons test in **A-B** and **E**, and by Kruskal-Wallis test with subsequent Dunn's multiple comparisons test in **D**.
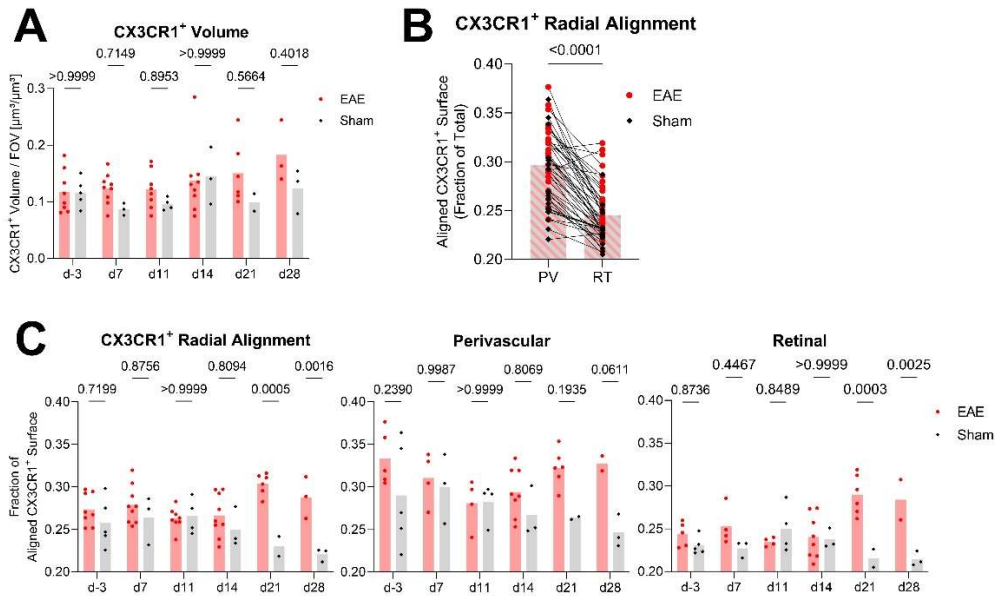
eFigure 6: In Vivo CX3CR1+ Cell Quantification

A, Graph shows measurements of CX3CR1+ volume per μm^3 of field of view (FOV). Data from Fig. 5B is broken down to single days post EAE induction. **B,** Graph shows comparison of radial alignment for perivascular macrophages (PV, defined by a distance of ≤ 10 μm from blood vessels) and retinal microglia (RT, defined by a distance of > 10 μm from blood vessels) acquired in the same volume, lines connect paired measurements. Edge pixels of CX3CR1+ surfaces are considered aligned if the spatial orientation of the respective edge differs less than ±20° from the polar angle of the edge, using a polar coordinate system with the ONH as pole for reference (as illustrated in Fig. 5C). **C,** Graphs show radial alignment measurements of CX3CR1+ surface edges. Left panel shows overall radial alignment, middle and left panels show radial alignment of perivascular and retinal cells, respectively. Data from Fig. 5D is broken down to single days post induction. Bars represent means. Statistical significance was determined by ordinary two-way ANOVA with subsequent Šídák's multiple comparisons test in **A** and **C**, and two-tailed Wilcoxon matched-pairs signed rank test in **B**.
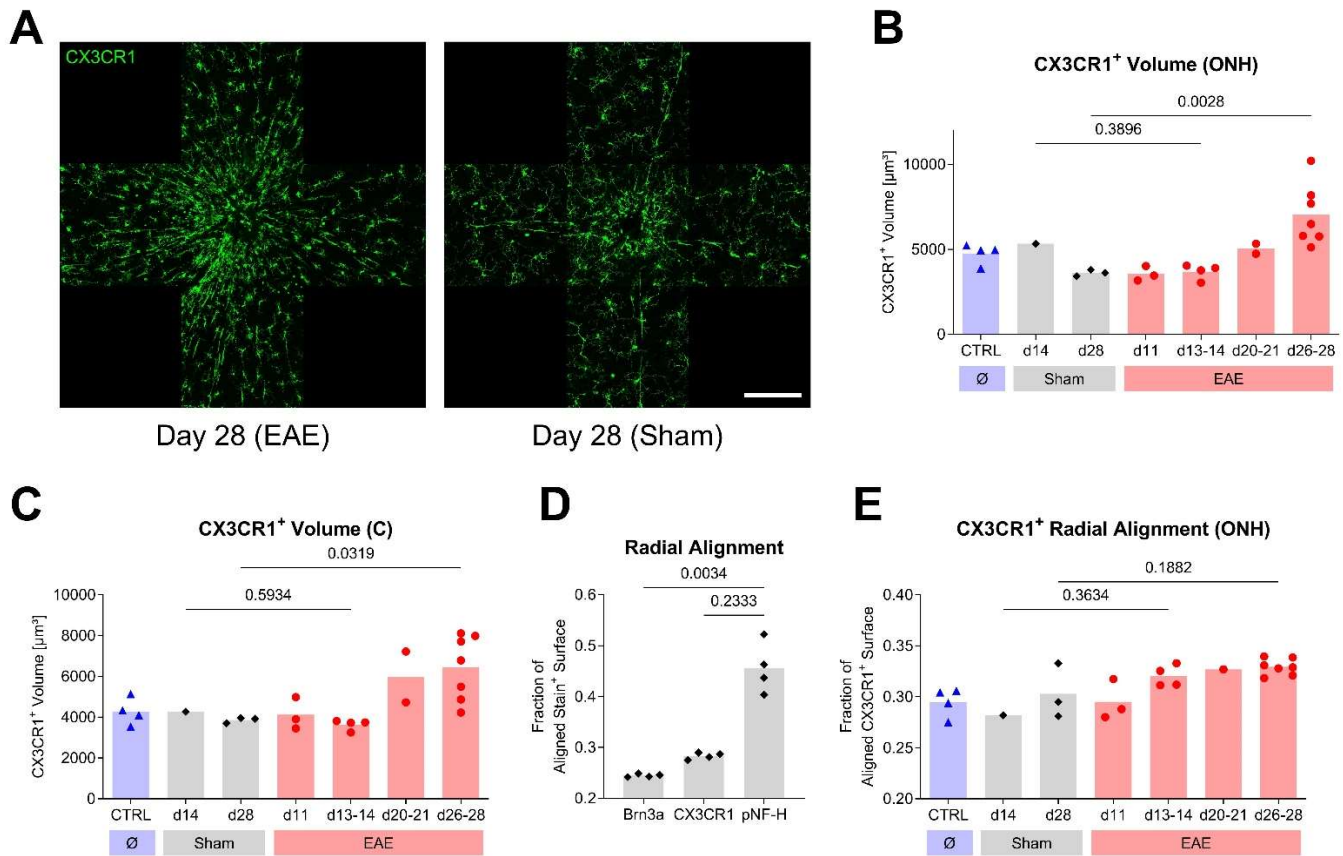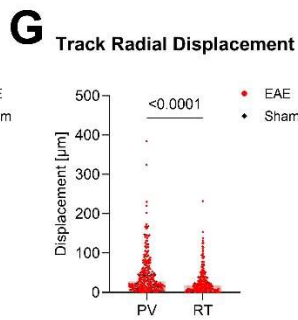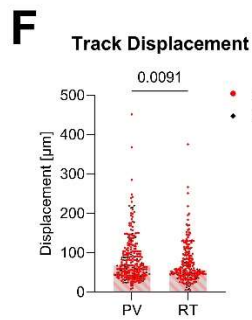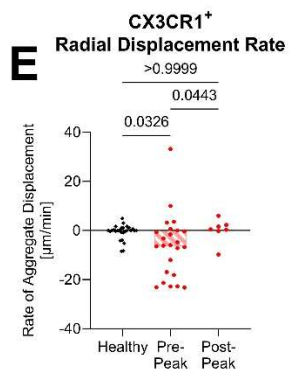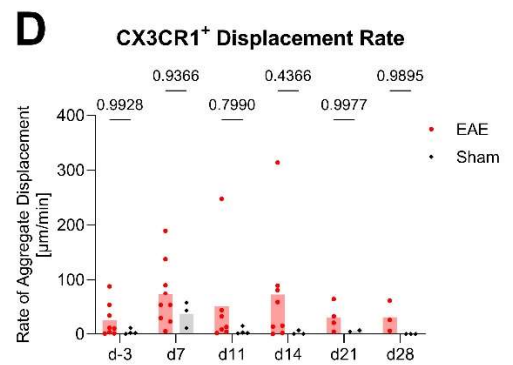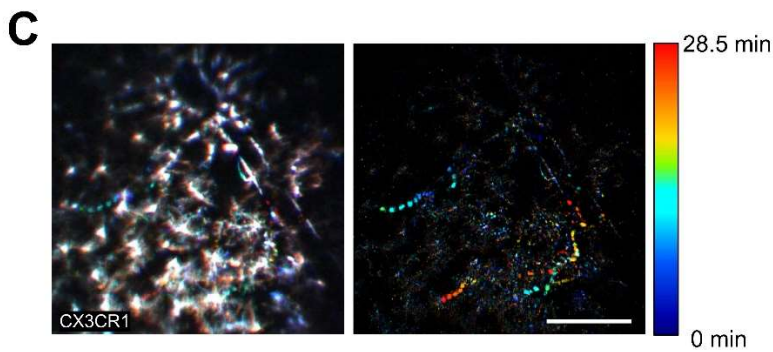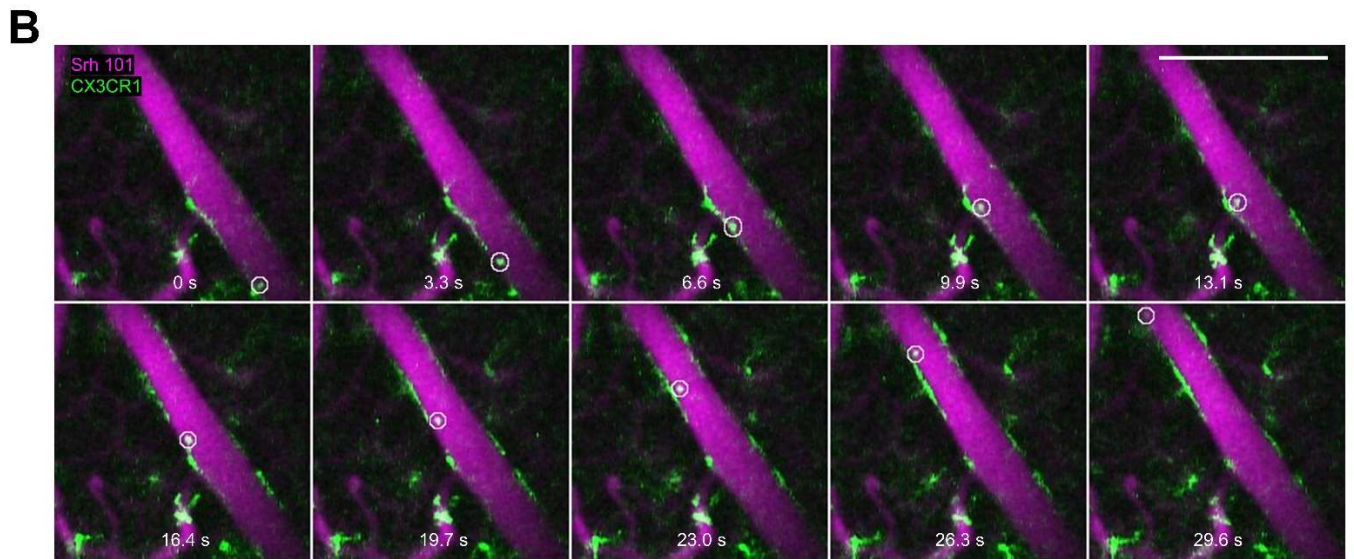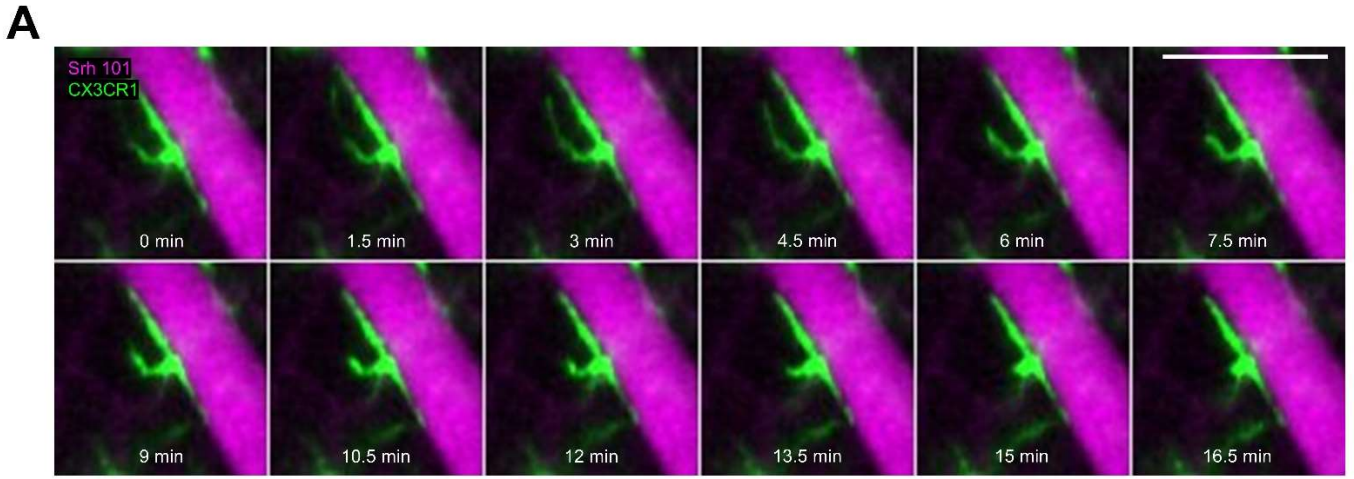
eFigure 7: CX3CR1⁺ Cell Quantification in Retinal Flatmounts

A, Montage of confocal microscopy images acquired in optic nerve head (ONH) and central retinal flatmount areas of representative experimental autoimmune encephalomyelitis (EAE, left panel) and sham treated (right panel) mice at 28 days post induction. CX3CR1⁺ microglia, monocytes and macrophages are shown in green. Scale bar represents 200 μm. Images are maximum projections of z-stacks. **B,** Graph shows measurements of CX3CR1⁺ volume in the ONH region for untreated control, sham injected and EAE mice, the latter two having been sacrificed at the indicated days post treatment. **C,** Graph shows measurements of CX3CR1⁺ volume in central retinal flatmount areas for untreated control, sham injected and experimental autoimmune encephalomyelitis (EAE) mice, the latter two having been sacrificed at the indicated days post injection. **D,** Graph compares radial alignment measurements in central retinal areas for different immunofluorescent stain patterns performed on the same central retinal flatmount areas of a healthy mouse, including Brn3a, a nucleic marker of retinal ganglion cells, CX3CR1, a marker of retinal microglia and macrophages, as well as pNF-H, an axonal marker. **E,** Graphs show radial alignment measurements of CX3CR1⁺ surface edges in the optic nerve head (ONH) region for untreated control, sham injected and EAE mice, the latter two having been sacrificed at the indicated days post induction (datapoints show mean of left and right eye). Edge pixels are considered aligned if the spatial orientation of the respective edge differs less than ±20° from the polar angle of the edge, using a polar coordinate system with the ONH as pole for reference (as illustrated in Fig. 5C). Datapoints in **B-C** and **E** represent means of measurements in left and right retina. Bars represent means. Statistical significance was determined by Kruskal-Wallis test with subsequent Dunn's multiple comparisons test.

A

Srh 101
CX3CR1

0 min 1.5 min 3 min 4.5 min 6 min 7.5 min

9 min 10.5 min 12 min 13.5 min 15 min 16.5 min

B

Srh 101
CX3CR1

0 s 3.3 s 6.6 s 9.9 s 13.1 s

16.4 s 19.7 s 23.0 s 26.3 s 29.6 s

C

CX3CR1

28.5 min

0 min

D CX3CR1⁺ Displacement Rate

0.9928 0.9366 0.4366 0.9895
0.7990 0.9977

Rate of Aggregate Displacement [µm/min]

d-3 d7 d11 d14 d21 d28

● EAE
◆ Sham

E
CX3CR1⁺
Radial Displacement Rate

>0.9999
0.0443
0.0326

Rate of Aggregate Displacement [µm/min]

Healthy Pre-Peak Post-Peak

F Track Displacement

0.0091

Displacement [µm]

PV RT

● EAE
◆ Sham

G Track Radial Displacement

<0.0001

Displacement [µm]

PV RT

● EAE
◆ Sham

eFigure 8: In Vivo CX3CR1⁺ Cell Tracking (Legend on the following page)

eFigure 8: In Vivo CX3CR1$^+$ Cell Tracking

A, Montage of timelapse two-photon microscopy (2PM) imaging in a healthy mouse, representative of CX3CR1$^+$ cell process dynamics observable in retinal 2PM imaging. Single images are sum projections of z-stacks. Blood vessels, stained with sulforhodamine 101 (Srh 101), are shown in magenta. CX3CR1$^+$ cells are shown in green. **B,** Montage of z-stack acquired using two-photon microscopy (2PM) in a healthy mouse, representative of CX3CR1$^+$ cellular movement observable even within a standalone z-stack, as acquiring each single image in a stack took approx. 3.3 s. Blood vessels, stained with sulforhodamine 101 (Srh 101), are shown in magenta. CX3CR1$^+$ cells are shown in green. The same cell is circled in each image. **C,** Time color-coded display of timelapse 2PM imaging in a healthy *CX3CR1.EGFP* mouse. Right panel shows data from left panel after subtraction of intensity values of each timepoint t_n from its following timepoint t_{n+1}, thus eliminating all stationary elements and facilitating single CX3CR1$^+$ cell tracking in the remainder (see Supplementary Methods). **D,** Graph shows displacement rate of CX3CR1$^+$ cells. Individual datapoints represent aggregate displacement rate of all CX3CR1$^+$ cells registered over the course one imaging session. Data from Fig. 7B is broken down to single days post induction. **E,** Graph shows radial displacement rate of CX3CR1$^+$ cells. Individual datapoints represent aggregate radial displacement rate of all CX3CR1$^+$ cells registered over the course one imaging session. Same data as in Fig. 7C, grouped as indicated in eFigure 2A. **F,** Graph shows comparison of total displacement of single perivascular (PV, defined by a distance of ≤ 10 µm from blood vessels) versus retinal (RT, defined by a distance of > 10 µm from blood vessels) CX3CR1$^+$ cells. **G,** Graph shows comparison of radial displacement of single perivascular versus retinal CX3CR1$^+$ cells. Scale bar in **A** represents 100 µm, scale bars in **B-C** represent 200 µm. Bars represent means. Statistical significance was determined by ordinary two-way ANOVA with subsequent Šídák's multiple comparisons test in **D**, Kruskal-Wallis test with subsequent Dunn's multiple comparisons test in **E**, and two-tailed Mann-Whitney test in **F-G**.